nature communications

Article

https://doi.org/10.1038/s41467-025-60324-0

Conformal hexagonal boron nitride encapsulation of graphene-skinned glass fiber fabric for enhanced electrical stability

Received: 10 December 2024

Accepted: 21 May 2025

Published online: 28 May 2025

Check for updates

Xiaomin Yang[1,7], Yuyao Yang[1,2,7], Shuting Cheng[1,3,7], Hao Yuan[1,2], Xuzhao Gai[1], Wenjuan Li[1,2], Fushun Liang[1,2], Fan Yang[1,2], Kangyi Zheng[1,4], Longfei Liu[1,5], Wenjing Jiang[1,6], Qingxu Su[1,2], Xinyu Mao[1], Jingnan Wang[1], Yuejie Zhao[1], Enshan Liu[1], Zhongfan Liu[1,2] ✉ & Yue Qi[1] ✉

Encapsulation is crucial for protecting graphene devices, but traditional whole-package encapsulations usually add bulky structures and reduce their flexibility. Hexagonal boron nitride (*h*-BN) holds potential for graphene encapsulation, but faces challenges in large-area acquisition and conformal coverage due to limitations in exfoliation and transfer techniques. Graphene-skinned glass fiber fabric (GGFF), made via graphene CVD growth on each fiber of a glass fiber fabric, consists of a hierarchical conductive network, but pressure/deformation-induced inter-fiber contact resistance fluctuations destabilize its electrical conduction. Whole-package encapsulation cannot resolve this, as fails to insulate inter-fiber contacts. Herein, thick, high-quality *h*-BN films are CVD-grown on each fiber in GGFF, achieving conformal encapsulation. This unlocks conductive network in GGFF, stabilizing electrical conduction while preserving structure stability and flexibility. This also improves GGFF's resistance to doping and oxidation, extending its service life. This encapsulation strategy is broadly applicable to other two-dimensional materials and complex device structures, promoting reliable nanoelectronics in demanding environments.

Graphene is highly sensitive to the environmental factors due to its special physical and electronic structures[1,2]. It is easily doped by water vapor and oxygen in air, leading to performance discrepancies and degradation[3–5]. For graphene electronic devices, encapsulation is a significant solution to resist the effects of external environmental factors. Currently, commonly used encapsulation materials for graphene devices include polymers[6,7], ceramics[8,9], and *h*-BN[10–12]. These encapsulation materials are typically applied to the surface of graphene layers through coating or stacking. However, these traditional encapsulation approaches are plagued by issues including flexibility loss and thickness increase[13]. It is important to note that these conventional encapsulation strategies typically involve covering the entire graphene layers or the entire device as a whole. Consequently, for graphene materials/devices with intricate and hierarchical structures,

[1]Beijing Graphene Institute (BGI), Beijing 100095, China. [2]Centre for Nanochemistry, Beijing Science and Engineering Centre for Nanocarbons, Beijing National Laboratory for Molecular Sciences, College of Chemistry and Molecular Engineering, Peking University, Beijing 100871, China. [3]School of Population and Health, Renmin University of China, Beijing 100872, China. [4]College of Energy, Soochow Institute for Energy and Materials Innovations (SIEMIS), Jiangsu Provincial Key Laboratory for Advanced Carbon Materials and Wearable Energy Technologies, Soochow University, Suzhou 215006, China. [5]Academy for Advanced Interdisciplinary Research, North University of China, Taiyuan 030051, China. [6]Department of Chemistry, School of Light Industry Science and Engineering, Beijing Technology and Business University, Beijing 100048, China. [7]These authors contributed equally: Xiaomin Yang, Yuyao Yang, Shuting Cheng. ✉e-mail: zfliu@pku.edu.cn; qiyue@bgi-graphene.com

this whole-package encapsulation disregards their macro/micro structures, which will compromise or even sacrifice the intrinsic structural advantages of materials/devices and impact their unique and specialized applications.

Graphene-skinned glass fiber fabric (GGFF) is a composite material developed by our group, where graphene is chemical vapor deposition (CVD)-grown on each fiber in glass fiber fabric (GFF) like skins[14–16]. GGFF combines the properties of graphene and glass fiber, such as the high electrical and thermal conductivities of graphene, along with the remarkable mechanical strength and flexibility of glass fiber. GGFF presents promising potentials applied in the areas such as electric heating anti-/de-icing and electromagnetic interference shielding[17–20]. Notably, GGFF features a hierarchical structure woven from warp and weft yarns in a plain weave form, and each yarn is composed of thousands of conductive graphene-skinned glass fibers (GGFs). Thus, a conductive network is constructed in GGFF. Consequently, when subjected to external pressure/deformation, the contact resistances between the conductive GGFs will be changed, leading to the unintended fluctuations in the overall conduction of GGFF. This will affect the function stability of the conductive fabric in practical applications. Unfortunately, even though the traditional whole-package encapsulation can achieve the encapsulation of the entire fabric as a whole, it fails to realize the effective insulation of individual conductive fibers in the fabric. Therefore, the issue of instable electrical conduction of GGFF caused by the unintended electrical contacts between fibers cannot be resolved by the conventional whole-package encapsulation strategies. In this situation, GGFF offers an ideal platform for developing advanced encapsulation strategies applied in hierarchical or intricately shaped conductive structures.

h-BN is a commonly used encapsulating material for graphene because of its atomically flat surface, similar lattice structure, and high stability[11,12,21,22]. However, large-area acquisition of *h*-BN films remains restricted by current preparation and transfer techniques, *i.e.* exfoliation from bulk materials or transferring from CVD-grown samples[23,24]. More importantly, encapsulation using above ex-situ *h*-BN films often fails to provide a conformal coverage for intricately shaped graphene materials/devices, where *h*-BN films are difficult to perfectly adhere to the surfaces of intricate structures[25], facing the same issues as the whole-package encapsulation. An effective strategy to address this issue is to in-situ grow *h*-BN layers on target graphene structures, where *h*-BN can realize the bottom-up deposition on the surface. However, constrained by current preparation techniques, particularly on noncatalytic substrates, the CVD growth of high-quality, large-area, and thick *h*-BN layers still poses significant challenges, limiting the implementation of this strategy[26,27].

In this work, with GGFF as a representative platform featuring intricate and hierarchical structure, the conformal encapsulation for each conductive fiber in large-area fabric is realized through in-situ CVD growth of high-quality, thick *h*-BN layers. This is challenging due to the noncatalytic nature of GGFs. This *h*-BN encapsulation effectively insulates the random electrical contacts between conductive fibers in GGFF, unlocking the conductive network in the fabric structure. Consequently, when external pressure/deformation is applied, although the contacts between fibers fluctuate, their contact resistances barely change, ensuring the stable electrical conduction of GGFF. Notably, the characteristic weaving structure and flexibility of GGFF are still well-preserved after encapsulation. Additionally, *h*-BN films offer a barrier against water vapor and oxygen in the atmospheric environment, enhancing the reliability and durability of GGFF during practical applications. This *h*-BN encapsulation technology is highly scalable and universal, which can be expanded to other two-dimensional materials and complicated device structures. This will advance the development of nanoelectronics with intricate architectures and extend their applications in complex operational environments.

Results

CVD growth of *h*-BN layers on each fiber in GGFF

GGFF is obtained through graphene CVD growth on each glass fiber in GFF, as schematically shown in Fig. 1a (left), and the mass production of GGFF has been realized by our group[14,18]. After obtaining GGFF, *h*-BN is then conformally deposited on each graphene-covered glass fiber in GGFF through the high-temperature decomposition of ammonia borane (BH_3NH_3), as shown in Fig. 1a (right) (see more details on the preparation progresses of GGFF and *h*-BN encapsulated GGFF (*h*-BN/GGFF) in Methods section and Supplementary Fig. 1). Figure 1b shows the photographs of GGFF (left) and *h*-BN/GGFF (right) with an area of $5 \times 12\ cm^2$, where the uniform contrasts observed on the two samples indicate the large-area uniform deposition of graphene and *h*-BN layers. Scanning electron microscopy (SEM) image demonstrates the well-defined fibrous structure of *h*-BN/GGFF (Fig. 1c). The intermediate growth stages of *h*-BN on graphene-covered fibers in GGFF were also investigated (Supplementary Figs. 2-4). With the growth time extending, the domain size and density of *h*-BN progressively increased, leading to the conformal growth of continuous *h*-BN films on the fibers with the good surface smoothness in GGFF (Supplementary Fig. 5). Energy dispersive X-ray spectrometry (EDS) elemental mappings of individual *h*-BN-encapsulated GGF (*h*-BN/GGF) presents the uniform distributions of B, N, and C elements on each fiber (Fig. 1d). Additionally, the uniform distributions of B and N on GFF were further confirmed by the Auger electron spectroscopy (AES) characterization, reinforcing the conformal covering of continuous *h*-BN on the fiber surface in GGFF (Supplementary Fig. 6). Furthermore, the statistical evaluation of the quality and thickness of *h*-BN on outer and inner fibers in *h*-BN/GGFF demonstrates a uniform growth of *h*-BN within the three-dimensional hierarchical structure of the fabric (see more details in Supplementary Fig. 7). These results confirm the conformal deposition of *h*-BN and graphene layers on each glass fiber in the fabric.

Figure 1e and f present the cross-section high-resolution transmission electron microscopy (HR-TEM) image of *h*-BN/GGF and the corresponding contrast profile, respectively. The HR-TEM presents the well-defined layered structures of *h*-BN and graphene, which are well aligned along the substrate surface. From the interlayer distances observed in the contrast profile in Fig. 1f, *h*-BN (~0.33 nm) and graphene (~0.38 nm) layers can be clearly distinguished. This suggests ~27 layers *h*-BN are deposited on ~2 layers of graphene, consistent with the HR-TEM in Fig. 1e, presenting ~8.9 nm *h*-BN stacking on ~1.0 nm graphene. To further confirm the film thickness of *h*-BN on graphene, the cross section of *h*-BN/GGF is also analyzed using electron energy loss spectroscopy (EELS) (Fig. 1g) and EDS elemental mapping (Supplementary Fig. 8), which reveal the consistent results with that in Fig. 1e and f.

Figure 1h shows the HR-TEM image taken from the surface of *h*-BN/GGF, where the well-defined Moiré patterns are clearly visible (see more details in Supplementary Fig. 9). The corresponding fast Fourier transform (FFT, inset in Fig. 1h) and selected area electron diffraction (SAED, Supplementary Fig. 10) patterns reveal multiple sets of distinct six-membered diffraction spots. These results confirm the high-quality graphene and *h*-BN stacking layers in *h*-BN/GGFF. Raman spectroscopy was employed to assess the quality of graphene before and after *h*-BN deposition. As shown in Fig. 1i, GGFF displays the characteristic Raman peaks of graphene at ~1350 cm^{-1} (D band), ~1590 cm^{-1} (G band), and ~2690 cm^{-1} (2D band), with the intensity ratio of D and G peaks (I_D/I_G) of ~0.24 and the intensity ratio of 2D and G peaks (I_{2D}/I_G) of ~1.28. After *h*-BN growth, I_D/I_G and I_{2D}/I_G of *h*-BN/GGFF show negligible change, indicating that the quality and thickness of graphene layers is barely affected by *h*-BN growth. Notably, a significant asymmetry in the peak within 1250-1450 cm^{-1} range in Raman spectra of *h*-BN/GGFF is

https://doi.org/10.1038/s41467-025-60324-0

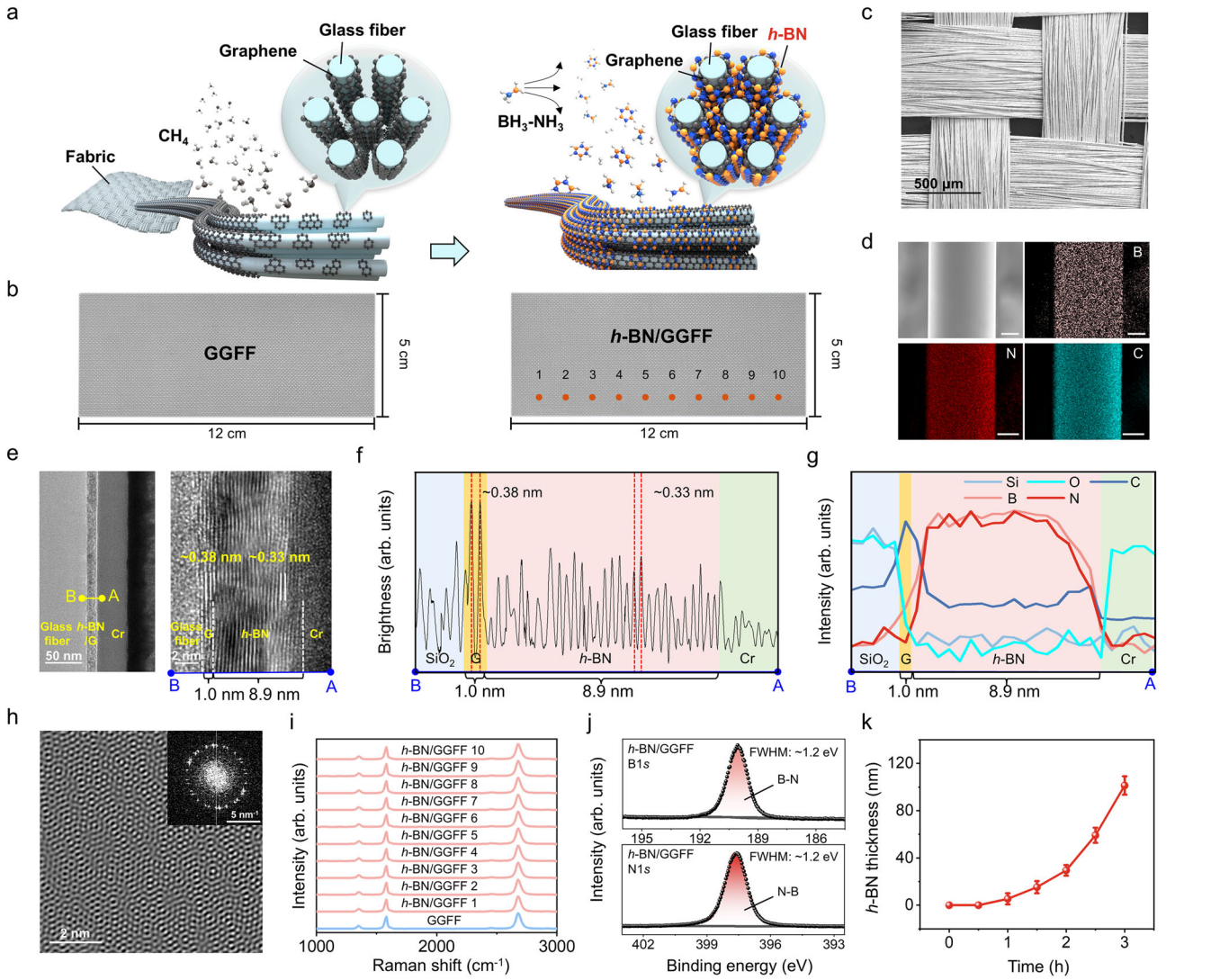

Fig. 1 | Preparation of graphene-skinned glass fiber fabric (GGFF) and hexagonal boron nitride (*h*-BN) encapsulated GGFF (*h*-BN/GGFF). **a** Schematics for the chemical vapor deposition (CVD) growth of graphene on glass fiber fabric (GFF) to obtain GGFF (left) and CVD growth of *h*-BN on GGFF to obtain *h*-BN/GGFF (right). **b** Photographs of GGFF (left, 5 × 12 cm^2, with graphene thickness of ~1.0 nm) and *h*-BN/GGFF (right, 5 × 12 cm^2, with graphene and *h*-BN thickness of ~1.0 nm and ~8.9 nm, respectively). **c** Scanning electron microscope (SEM) image of *h*-BN/GGFF. **d** Energy dispersive spectrometer (EDS) elemental mappings of B, C, and N elements of *h*-BN/GGF (scale bar, 2 μm). **e** Cross-section high resolution-transmission electron microscope (HR-TEM) image of *h*-BN/GGF. The regions of glass fiber, *h*-BN/G (*h*-BN stacking on graphene (G)), and chromium (Cr) protection layer are labeled. **f** Contrast profile along the blue line in **e**. The vertical red dashed lines mark characteristic interlayer distances of graphene or *h*-BN. **g** Line scan analysis of electron energy loss spectroscopy (EELS) along the blue line in (**e**). The blue, yellow, red, and green areas in **f**, **g** represent SiO_2 substrate, graphene, *h*-BN, and Cr protection layers, respectively. **h** HR-TEM image on *h*-BN/GGF and its corresponding fast Fourier transform (FFT) pattern (inset). **i** Raman spectra collected from the marked positions on *h*-BN/GGFF in **b** (right). Raman spectrum of original GGFF was also included for comparison. **j** X-ray photoelectron spectroscopy (XPS) core level spectra of B1*s* and N1*s* of *h*-BN/GGFF. **k** Thickness of *h*-BN layers in *h*-BN/GGFF obtained with different growth times of *h*-BN. The error bars represent the standard deviations ($n = 5$).

observed (Supplementary Fig. 11), suggesting the convolution of the D band of graphene and the E_{2g} band of *h*-BN. After peak deconvolution, the graphene D band and *h*-BN E_{2g} band are distinguished, which further confirms the covering of *h*-BN on graphene. As shown in Fig. 1j, the X-ray photoelectron spectroscopy (XPS) core-level spectra show the characteristic B1*s* (~190.4 eV) and N1*s* (~397.9 eV) peaks of *h*-BN in *h*-BN/GGFF, with an intensity ratio of 1:1, which are in accordance with reported XPS characterization of *h*-BN[28]. Based on the analysis of the C1*s* spectra of GGFF and *h*-BN/GGFF, no B-C or N-C bonding is formed at the interface of *h*-BN/graphene heterostructure (see more details in Supplementary Fig. 12). Additionally, the thickness of *h*-BN layers in *h*-BN/GGFF can be regulated by its growth time. As shown in Fig. 1k, by controlling the growth time of *h*-BN from ~0.5 to ~3 hours, the thickness can be adjusted from ~5.4 to ~101.3 nm (corresponding to the layer number from ~16 to ~307) (see more details on the thickness measurement of *h*-BN layers in Methods section and Supplementary Fig. 13). The accelerated increase in *h*-BN thickness over time is attributed to the progressively increased concentration of active species, which accelerates the growth process of *h*-BN (see more details in Supplementary Figs. 14 and 15). Additionally, the preparation progresses of GGFF and *h*-BN/GGFF demonstrate high batch-to-batch stability. As shown in Supplementary Figs. 16 and 17, graphene and *h*-BN grown across multiple batches exhibit remarkable consistency in both quality and thickness. This stability serves as a critical foundation for the scalable fabrication of devices in practical applications. It is worth mentioning that CVD growth of *h*-BN with high quality and thick layers is critical for the ideal insulation and encapsulation, but it is challenging, especially on the noncatalytic substrate surfaces.

https://doi.org/10.1038/s41467-025-60324-0

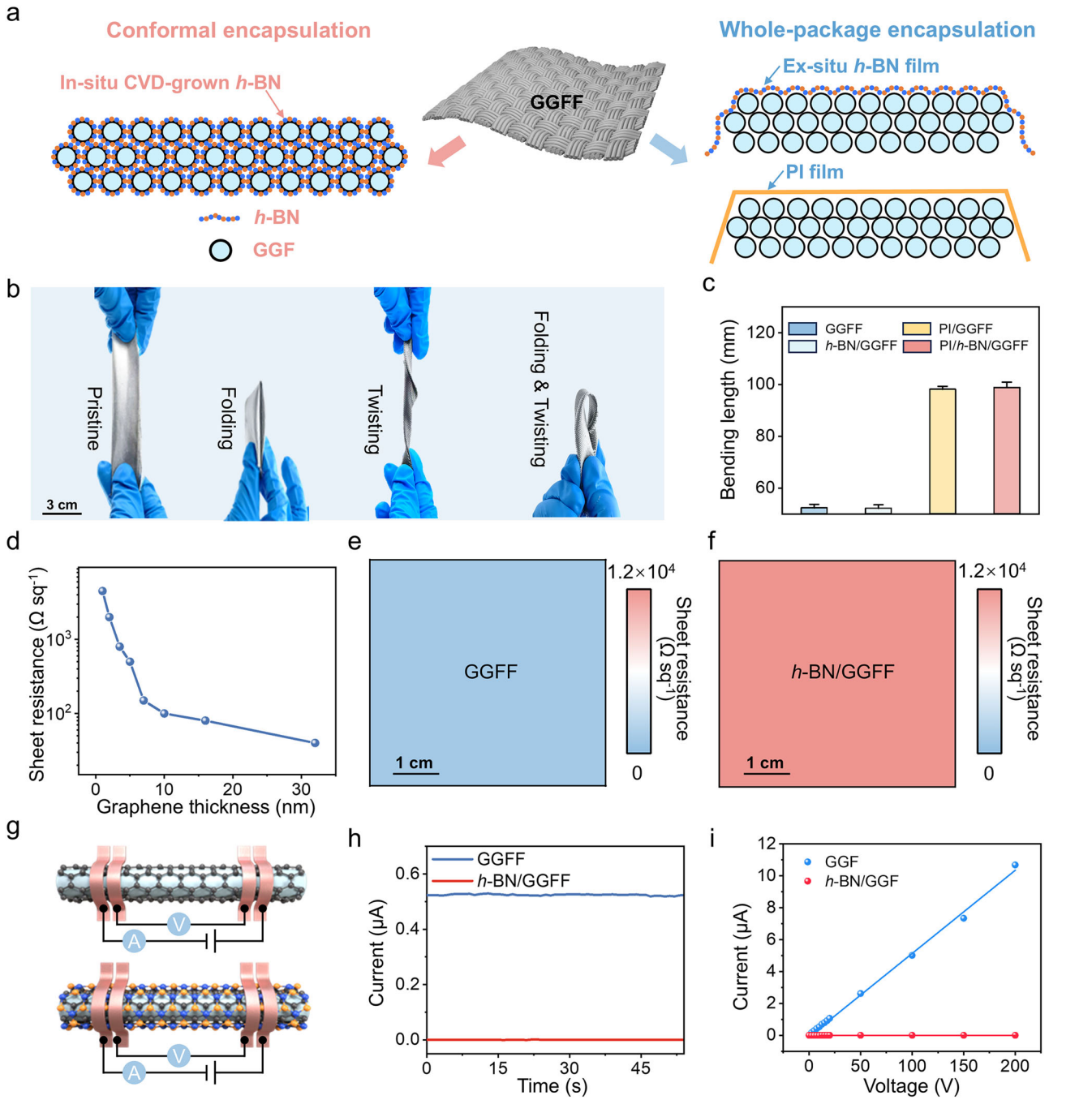

Fig. 2 | Mechanical and electrical properties of GGFF and *h*-BN/GGFF. **a** Schematics for the conformal encapsulation by in-situ CVD-grown *h*-BN (left), and the whole-package encapsulation by ex-situ *h*-BN and polyimide (PI) film (right). **b** Photographs of *h*-BN/GGFF (25 × 120 mm^2) under a series of mechanical deformations, showing the high flexibility. **c** Bending length of GGFF, *h*-BN/GGFF, PI/GGFF, and PI/*h*-BN/GGFF. GGFFs used have graphene thickness of ~1.0 nm, and *h*-BN/GGFF used have graphene and *h*-BN thickness of ~1.0 nm and ~50.4 nm, respectively. The error bars represent the standard deviations (n = 5). **d** Sheet resistance of GGFF at varying thickness of graphene. Sheet resistance mappings of GGFF (**e**) and *h*-BN/GGFF (**f**). In **e**, **f**, the size of GGFF and *h*-BN/GGFF is 5 × 5 cm^2. GGFF has graphene thickness of ~1.0 nm, and *h*-BN/GGFF has graphene and *h*-BN thickness of ~1.0 nm and ~29.5 nm, respectively. Sheet resistance values were measured using a four-point probe with 0.5 cm step size in both x- and y-directions. **g** Schematics of the test devices based on GGF and *h*-BN/GGF. **h** Current flowing through GGF and *h*-BN/GGF test devices in **g** under the input voltage of 10 V. **i** Electrical transport measurements (current-voltage (I-V) curves) of GGF and *h*-BN/GGF test devices in **g** for voltages ranging from 0 V to 200 V. In **g**–**i**, the length of GGF and *h*-BN/GGF is ~0.5 cm. GGF has graphene thickness of ~1.0 nm, and *h*-BN/GGF has graphene and *h*-BN thickness of ~1.0 nm and ~50.4 nm, respectively.

Mechanical and electrical properties of *h*-BN/GGFF

In *h*-BN/GGFF, the in-situ CVD-grown *h*-BN layers allows for the direct growth of *h*-BN layers on each GGF in the fabric, ensuring a high degree of conformality and minimizing defects, as schematically shown in Fig. 2a (left). In contrast, as schematically shown in Fig. 2a (up right), the ex-situ *h*-BN layers, which are exfoliated from the bulk material or transferred from CVD-grown samples, encapsulate the fabric in a whole-package form. This approach may introduce more defects due to the transfer process. In addition to *h*-BN, organic polymer materials, such as polypropylene[6], polyethene[29], polyurethane[30], poly-(vinylidene chloride)[7], and polyimide (PI)[31] are also commonly used in the encapsulation of conductive devices because of their insulating property and

low cost. To compare with *h*-BN conformal encapsulation, PI film encapsulation for GGFF is also introduced in this study for comparison, as schematically shown in Fig. 2a (bottom right). Like the ex-situ *h*-BN layers, PI film also encapsulates GGFF in a whole-package form.

h-BN/GGFF retains the high intrinsic flexibility of GFF and GGFF, which can be twisted and folded arbitrarily (Fig. 2b), Negligible change in morphology and no peeling of *h*-BN/graphene layers are observed after the repeated deformations (Supplementary Fig. 18). In contrast, GGFF encapsulated by PI film (PI/GGFF) loses the flexibility, becoming much more rigid than GGFF (Supplementary Fig. 19). The bending length is commonly used to quantitatively assess the flexibility of materials (see more details about the measurement in Supplementary Fig. 20). The smaller bending length indicates the higher flexibility. From Fig. 2c, it can be observed that GGFF and *h*-BN/GGFF exhibit a similar bending length of ~52 mm, both of which are much smaller than that of PI/GGFF and *h*-BN/GGFF encapsulated by PI film (PI/*h*-BN/GGFF), which bending length is ~98 mm. This indicates that *h*-BN conformal encapsulation doesn't lower the flexibility of GGFF, in contrast, PI film encapsulation significantly compromises GGFF's flexibility. Additionally, *h*-BN conformal encapsulation on each fiber in GGFF also effectively enhanced the tensile strength of the fabric (see more details in Supplementary Fig. 21).

GGFF exhibits electrical conduction due to graphene covering each fiber in the fabric, which can be effectively regulated by controlling the thickness of graphene layers. As shown in Fig. 2d, the sheet resistance of GGFF decreases with the thickness increase of graphene layers. Figure 2e shows the sheet resistance mapping of GGFF, exhibiting a uniform conduction with an average value of ~400 Ω sq^{-1} (with graphene thickness of ~1.0 nm). After *h*-BN encapsulation (with thickness of ~29.5 nm), the measured sheet resistance of *h*-BN/GGFF increases high to ~1.2 × 10^4 Ω sq^{-1} (Fig. 2f), and when *h*-BN thickness reaches ~50.4 nm, the sheet resistance of *h*-BN/GGFF exceeds the detection limit (10^{-3}–10^6 Ω sq^{-1}) of the four-probe tester (RTS-8). This proves the insulation effect of the prepared *h*-BN layers. To further verify that *h*-BN conformal encapsulation can effectively insulate each conductive fiber in GGFF, the test devices based on GGF and *h*-BN/GGF (with graphene and *h*-BN thickness of ~1.0 nm and ~50.4 nm, respectively) were constructed as shown in Fig. 2g (see more details for the device construction in Supplementary Fig. 22). Figure 2h illustrates that when a voltage of 10 V is applied to the test devices, the static-state current through GGF remains stable at ~0.5 μA, while almost no current flows through *h*-BN/GGF. Figure 2i presents the current-voltage (I-V) curves of the test devices in a voltage range of 0–200 V. For GGF, the current increases linearly with the voltage, while it remains zero for *h*-BN/GGF. These results demonstrate that the *h*-BN layers can effectively insulate the conductive fibers within GGFF.

h-BN encapsulation, unlocking the conductive network in GGFF

GGFF is woven from weft and warp yarns in a plain texture, and each yarn comprises thousands of conductive fiber filaments, forming a typical hierarchical conductive network in the fabric. Figure 3a and b schematically illustrate the primitive module of the conductive network in GGFF. The current, as labeled by the arrow, is assumed to flow into the fabric along the warp direction. The electrical conduction of GGFF is influenced by the resistance of each fiber (R_0), the contact resistance between adjacent fibers (R_{c1}), the resistance of the warp (R_{warp}) and weft (R_{weft}) yarns, and the contact resistance between warp and weft yarns (R_{c2}). The equivalent circuit diagrams for current flowing within/between the yarns and fibers in the fabric are modeled in Fig. 3c and d, respectively. Specifically, as shown in Fig. 3d, the resistance of the warp or weft yarn (R_{warp} or R_{weft}) is affected by the inherent resistance of each fiber (R_0) and the contact resistance (R_{c1}) between adjacent fibers, which is caused by the random contacts between fibers. Additionally, in the whole fabric, besides R_{warp} and R_{weft}, fabric's resistance is also affected by the contact resistance between warp and weft yarns (R_{c2}), as shown in the equivalent circuit diagram in Fig. 3c.

The contact resistance in the fabric (R_{c1} and R_{c2}) can be evaluated via Holm's theory[32], using

$$R_c = \frac{\rho}{2}\sqrt{\frac{\pi H}{nP}} \tag{1}$$

where ρ is the electrical resistivity, H is the material hardness, n is the number of contact points, and P is the contact pressure. Factors such as external mechanical stress (including pressing, bending, or vibration) will affect the number of contact points (n) and contact pressure (P), thereby influencing the contact resistances (R_{c1} and R_{c2}) and thus the overall conduction of GGFF. Figure 3i shows a folded GGFF bearing weight load, and its total resistance is measured (see more details for the fabrication method of the electronic testing devices in the Methods section). As shown in Fig. 3j, GGFF's resistance decreases over 400 Ω (from ~1160 Ω to ~736 Ω) as the load weight increases to 20 g. This behavior is attributed to the changes in contact resistances between fibers (R_{c1}) and between yarns (R_{c2}) under varying pressures. This fluctuation in electrical conduction of GGFF will significantly impact the performance, reliability, and stability of the conductive fabric in practical applications.

The conformal encapsulation of *h*-BN for each fiber in GGFF can effectively isolate and insulate the randomly contacted fibers, unlocking the conductive network in GGFF (Fig. 3e and f). The resulting circuit diagrams after *h*-BN encapsulation is depicted in Fig. 3g and h. In the circuits, the contact resistances between fibers (R_{c1}) and between yarns (R_{c2}) are regarded infinite due to thick-layer *h*-BN insulation, and only the resistances of fibers (R_0) and yarns (R_{warp}) are retained. In this unlocked conductive network, when external pressure/deformation is applied, although contacts between fibers and yarns change, the electrical conduction of the entire fabric will not be affected. Figure 3k displays the resistances of *h*-BN/GGFF under different weight loads. The results demonstrate that the resistance of *h*-BN/GGFF remains nearly unchanged under varying weight loads. This stability indicates that *h*-BN encapsulation can effectively insulate the conductive fibers in GGFF, eliminating the instability of the contact resistances under deformation/pressure, and thereby ensuring the electrical stability of the entire conductive configuration.

To investigate the effects of different encapsulation strategies (*h*-BN conformal encapsulation and PI film whole-package encapsulation) on the electrical stability of GGFF, the electronic test devices based on GGFF, *h*-BN/GGFF, PI/GGFF, and PI/*h*-BN/GGFF were constructed (see more details in Supplementary Fig. 23). Then the resistance change (ΔR) of GGFF under various mechanical deformations were monitored ($\Delta R = R' - R$, R representing initial resistance of GGFF, R' representing the resistance of GGFF when mechanical deformation is imposed, ΔR representing the resistance change of GGFF under mechanical deformation). Figure 3l–n show the resistance variations of GGFF, *h*-BN/GGFF, PI/GGFF, and PI/*h*-BN/GGFF under bending, pressing, and vibrating deformations, respectively. Figure 3l presents that under bending deformations at varying angles from 0° to 180°, significant decreases in GGFF's resistance are observed, and the resistance variation keeps increasing as the bending angle increases, with the maximum value of ~201 Ω (from ~580 Ω to ~379 Ω) at bending angle of ~180°. Notably, for PI/GGFF, a significant decrease in resistance is also observed during the bending test, indicating that the PI film whole-package encapsulation cannot eliminate the electrical instability of GGFF, as fluctuations in the contact resistances between fibers and between yarns still occur under pressure/deformation. For *h*-BN/GGFF, the resistance of GGFF shows negligible change during the bending test, so as to PI/*h*-BN/GGFF. Similar results are observed under the other two types of deformations (pressing and vibrating deformations)

https://doi.org/10.1038/s41467-025-60324-0

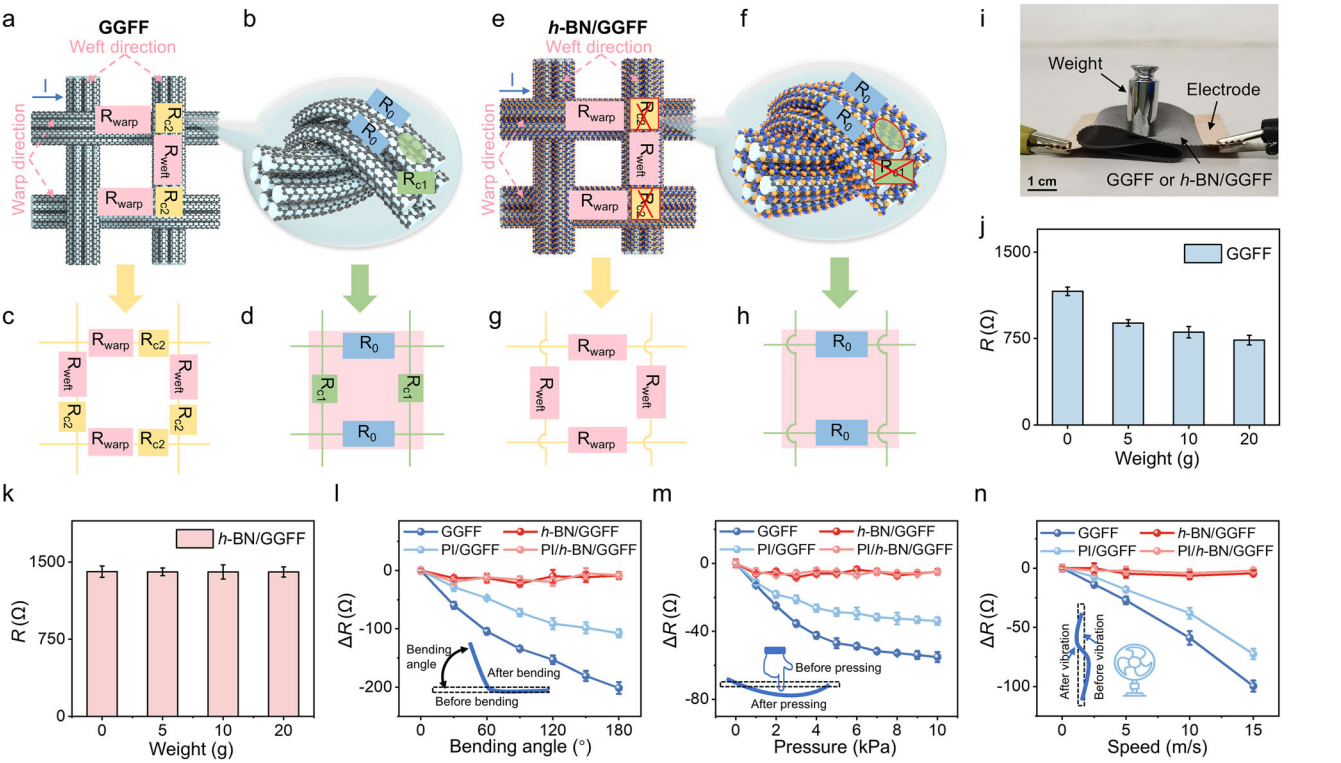

Fig. 3 | *h*-BN conformal encapsulation unlocking the conductive network in GGFF for enhanced electrical stability. Schematics for the conductive model constructed in GGFF (**a**, **b**) and corresponding equivalent circuits (**c**, **d**), where R_0 represents the resistance of each fiber, R_{warp} and R_{weft} represent the resistances of the warp and weft yarns, R_{c1} and R_{c2} represents the contact resistances between fibers and between warp and weft yarns. Schematics for the conductive model constructed in *h*-BN/GGFF (**e**, **f**) and corresponding equivalent circuits (**g**, **h**), where the resistances of R_{c1} and R_{c2} disappear as *h*-BN layers insulate the conductive GGFs. **i** Folded GGFF or *h*-BN/GGFF under weight load. Resistances of GGFF (**j**) and *h*-BN/GGFF (**k**) under different weight loads (0, 5, 10, 20 g). The size of GGFF and *h*-BN/GGFF is 5 × 10 cm^2. GGFF has graphene thickness of ~1.0 nm, and *h*-BN/GGFF has graphene and *h*-BN thickness of ~1.0 nm and ~50.4 nm, respectively. **l** Resistance change (Δ*R*) of GGFF, *h*-BN/GGFF, PI/GGFF, and PI/*h*-BN/GGFF under bending deformation at varying bending angles (Δ*R* = *R*′−*R*, *R* representing the initial resistance of GGFF, *R*′ represening the resistance of GGFF when mechanical deformation is imposed, Δ*R* representing the change of GGFF's resistance under mechanical deformation). Inset: Schematic depicting the bending deformation of the sample. **m** Resistance change (Δ*R*) of GGFF, *h*-BN/GGFF, PI/GGFF, and PI/*h*-BN/GGFF under pressing deformation at varying pressures. Inset: Schematic depicting the pressing deformation of the sample. **n** Resistance change (Δ*R*) of GGFF, *h*-BN/GGFF, PI/GGFF, and PI/*h*-BN/GGFF under vibrating deformation at different vibrating intensities. Inset: Schematic depicting the vibrating deformation of the sample. GGFFs used to prepare GGFF, *h*-BN/GGFF, PI/GGFF, and PI/*h*-BN/GGFF electronic test devices in **l**–**n** have size of 5 × 5 cm^2. GGFFs have a graphene thickness of ~1.0 nm, and *h*-BN/GGFFs have graphene and *h*-BN thickness of ~1.0 nm and ~50.4 nm, respectively. The structures for the test devices and the measurement progress are shown in Supplementary Fig. 23. The error bars in (**j**-**n**) represent the standard deviations (*n* = 5).

(Fig. 3m and n). The relative resistance variations (ΔR/R) of GGFF, *h*-BN/GGFF, PI/GGFF, and PI/*h*-BN/GGFF under bending, pressing, and vibrating deformations are also calculated based on Fig. 3l–n, as presented in Supplementary Fig. 24 for clearer illustration. These results show that external mechanical pressure/deformation can cause changes in the contacts between conductive fibers and between yarns in the fabric, thereby causing the instability in the overall electrical conduction of GGFF. PI film can realize the whole-package encapsulation of the entire fabric; however, it fails to insulate the conductive units (GGFs), and thus cannot solve the issue of electrical instability of the whole conductive configuration. *h*-BN conformal encapsulation for each fiber in the fabric effectively insulates randomly contacted conductive fibers, successfully unlocking the conductive network in GGFF. When external deformation is applied, although contacts between fibers change, the effects of contact resistance fluctuation are eliminated, thus ensuring the electrical stability of the overall circuit.

h-BN encapsulation enhancing resistance to water vapor

Graphene is highly susceptible to the adsorption of external molecules, particularly water vapor in the atmospheric environment, which leads to doping effects, thereby significantly impacts graphene's electrical properties[33–35]. Thick *h*-BN layers, not only provide insulation for the conductive fibers in GGFF, but also generate a labyrinth effect to extend the propagation path length of water vapor[36], as shown in Fig. 4a. Improved hydrophobicity can effectively repel water molecules and reduce their adherence to the fabric surface, as shown in Fig. 4b. As shown in Fig. 4c, the graphene coating improves the contact angle of GFF from ~10.2° to ~71.9°, demonstrating the superior hydrophobicity of GGFF. Moreover, *h*-BN coating (~ 15.3 nm) further enhances the hydrophobicity of the GGFF surface, with the contact angle increasing from ~71.9° to ~113.1°. This reduces the water penetration into the fabric's internal space, thereby minimizing the doping effects from water, and ultimately improving the fabric's electrical stability in the atmospheric environment.

The resistance changes (Δ*R*) of GGFF and *h*-BN/GGFF after ~8, ~24, ~48, ~72, ~120, and ~168 hours air exposure are systematically explored in Fig. 4d, where Δ*R* = *R*′ - *R*, *R* and *R*′ representing the initial resistance of fabric and the resistance with air exposure, respectively, and Δ*R* representing the resistance change of fabric with air exposure. It can be observed that the resistance of GGFF decreases rapidly during the first ~8 hours of air exposure, reaching the lowest point at ~24 hours and then remaining stable, with the maximum decrease >100 Ω (from ~580 Ω to 477 Ω). This conduction fluctuation of GGFF is due to the adsorbed-water-induced change in carrier concentration of graphene[34,37], which may cause the uncontrollable temperature, poor

https://doi.org/10.1038/s41467-025-60324-0

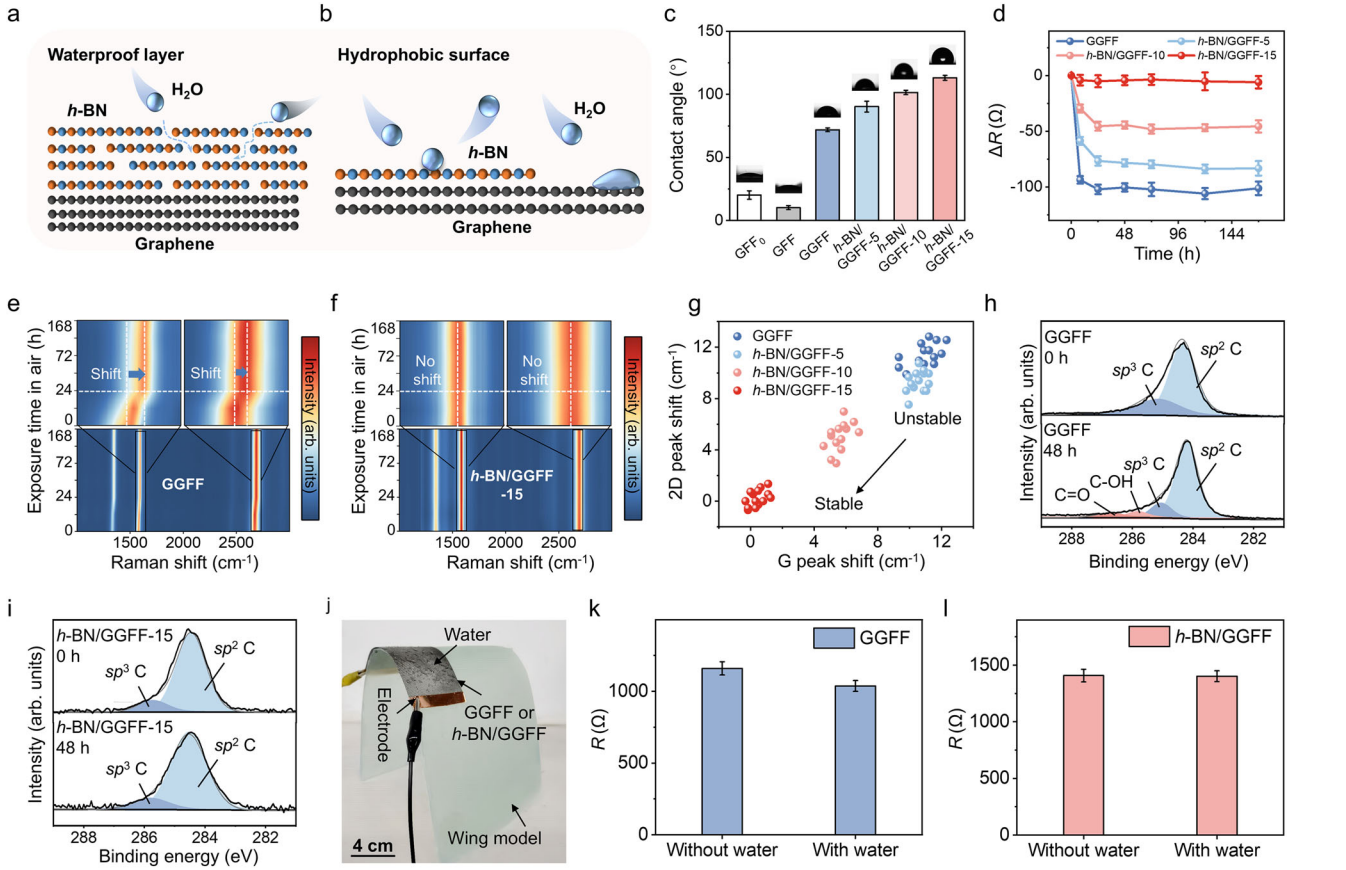

Fig. 4 | *h*-BN encapsulation enhances the electrical stability of GGFF against water vapor doping in atmospheric environment. Schematics for the labyrinth effect of *h*-BN barriers for the adsorbed water (**a**) and the enhanced hydrophobicity of GGFF after *h*-BN covering (**b**). **c** Water contact angle measurement of GFF_0, GFF, GGFF, *h*-BN/GGFF-5, *h*-BN/GGFF-10, and *h*-BN/GGFF-15. GFF_0 and GFF denote GFF before and after the removal of the polymer layer. GGFF has a graphene thickness of ~1.0 nm, *h*-BN/GGFF-5, *h*-BN/GGFF-10 and *h*-BN/GGFF-15 denote GGFFs encapsulated by *h*-BN with thickness of ~5.4, ~9.6 and ~15.3 nm, respectively. Inset: Contact angle images of GFF_0, GFF, GGFF, *h*-BN/GGFF-5, *h*-BN/GGFF-10, and *h*-BN/GGFF-15. **d** Resistance changes (ΔR) of GGFF, *h*-BN/GGFF-5, *h*-BN/GGFF-10, and *h*-BN/GGFF-15 upon ~8, ~24, ~48, ~72, ~120, ~168 hours of air exposure (~ 25 °C, atmospheric pressure). The size of sample is 5 × 5 cm^2. GGFF has graphene thickness of ~1.0 nm, *h*-BN/GGFF-5, *h*-BN/GGFF-10 and *h*-BN/GGFF-15 denote GGFFs encapsulated by *h*-BN layers with thickness of ~5.4, ~9.6 and ~15.3 nm, respectively. **e**, **f** Raman spectroscopy heatmaps of graphene in GGFF and *h*-BN/GGFF-15 after ~8, ~24, ~48, ~72, ~120, ~168 hours of air exposure (25 °C, atmospheric pressure). **g** Statistics for the shifts of Raman G and 2D peaks of graphene in GGFF, *h*-BN/GGFF-5, *h*-BN/GGFF-10 and *h*-BN/GGFF-15 after 48 hours of air exposure reletive to the intrinsic peak positions (~ 1582 cm^{-1} (G) and ~2680 cm^{-1} (2D)). XPS C 1*s* spectra of intrinsic GGFF (**h**) and *h*-BN/GGFF-15 (**i**) after 48 hours air exposure. **j** Resistance testing device for GGFF or *h*-BN/GGFF under the condition of water droplet deposition. The sample was conformally covered on the curved structure model, and water was sprayed on it. Resistances of GGFF (**k**) and *h*-BN/GGFF (**l**) before and after water spraying. The size of GGFF and *h*-BN/GGFF is 5 × 10 cm^2. GGFF has graphene thickness of ~1.0 nm, and *h*-BN/GGFF has graphene and *h*-BN thickness of ~1.0 nm and ~50.4 nm, respectively. The error bars in **c**, **d**, **k**, and **l** represent the standard deviations ($n = 5$).

electrothermal cycling stability, and unpredictable electrothermal performance of GGFF, ultimately limiting its practical applications. Noteworthy, the conduction fluctuation is alleviated by *h*-BN encapsulation. As shown in Fig. 4e, as the thickness of *h*-BN layers increases, the resistance decrease is relieved, and when *h*-BN thickness reaches ~15.3 nm (*h*-BN/GGFF-15), this electrical instability is negligible. Additionally, the resistance changes of GGFF and *h*-BN/GGFF upon exposure to a high humidity environment (~30 °C, ~70 % RH) were also investigated in Supplementary Fig. 25, which exhibits a more substantial decrease for GGFF, and the *h*-BN encapsulation can effectively alleviate this instability.

To investigate the doping effects of adsorbed water and the roles of *h*-BN barriers, Raman spectroscopic characterizations of GGFF and *h*-BN/GGFF-15 are performed, as shown in Fig. 4e and f. It can be noticed that after ~24 hours air exposure, both G and 2D peaks of graphene in GGFF shift to higher wavenumbers (~1590 cm^{-1} and ~2690 cm^{-1}, respectively) from the intrinsic positions obtained after just completing the growth process of graphene (~1580 cm^{-1} and ~2679 cm^{-1}, respectively). This implies the p-type doping of graphene caused by the water adsorption in air[38]. In contrast, negligible shifts in G and 2D peaks of graphene in *h*-BN/GGFF-15 are observed after being exposed in air for ~168 hours (Fig. 4f), confirming the barrier effect of *h*-BN layers. Figure 4g shows the statistics for the shifts of G and 2D peaks of graphene in GGFF, *h*-BN/GGFF-5, *h*-BN/GGFF-10, and *h*-BN/GGFF-15 after 48 h air exposure relative to the intrinsic peak positions. The results indicate that this p-type doping effect of water on graphene is significantly influenced by the thickness of *h*-BN layers. As *h*-BN thickness increases from ~5.4 to ~15.3 nm, the shifts of both G and 2D peaks gradually decrease, and for *h*-BN/GGFF-15, the shifts are nearly negligible. This indicates that thin layers of *h*-BN are not sufficient in preventing the doping effect of adsorbed water, and only thick *h*-BN layers exhibit ideal encapsulation effects. XPS characterizations of graphene further confirm the encapsulation by *h*-BN layers. The results in Fig. 4h and i show that freshly prepared GGFF and *h*-BN/GGFF display only sp^2- and sp^3-hybrided carbon peaks at ~284.3 eV and ~285.2 eV, respectively, are observed. However, after 48 hours air exposure, an additional two peaks at ~285.9 eV and ~286.6 eV corresponding to C–O and C=O bonds, respectively, appear in GGFF[39],

https://doi.org/10.1038/s41467-025-60324-0

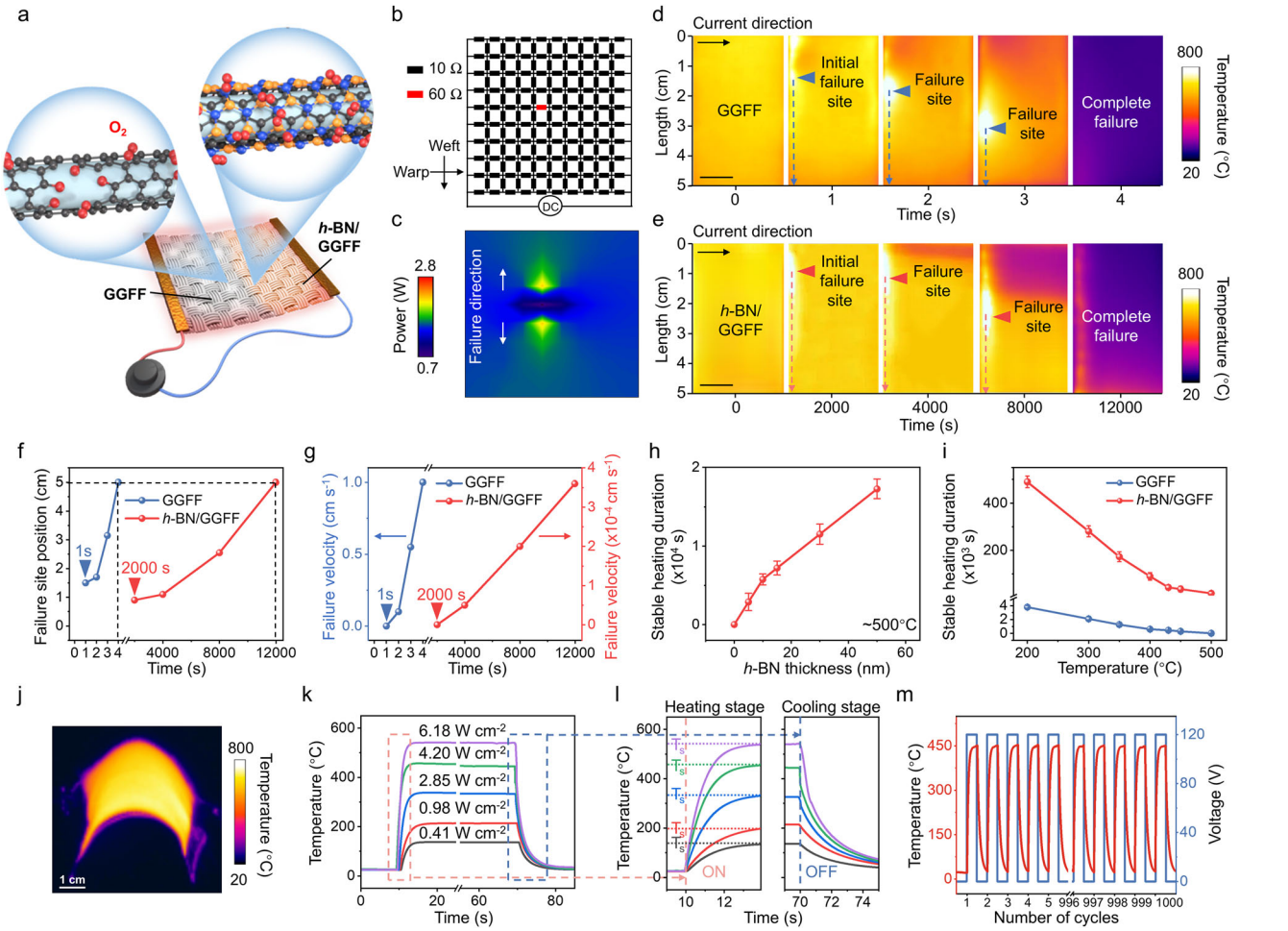

Fig. 5 | Performances of *h*-BN/GGFF electrothermal device in atmospheric environment. a Schematic for the oxidation progresses of GGFF and *h*-BN/GGFF electrothermal devices. **b** Simulated resistance network of GGFF electrothermal device composed of a series of resistance modules with resistance of 10 Ω (labeled in black color). One of the resistance modules is set higher (60 Ω, labeled in red color) to simulate defective location. The current flowing direction is along the warp direction of the fabric, as labeled in **b**. **c** Simulated electric power distribution of GGFF electrothermal device with the resistance network in **b** under an input voltage of 40 V. Infrared images of GGFF (**d**) and *h*-BN/GGFF (**e**) electrothermal devices during their failure processes (scale bar, 1 cm). The dashed arrows denote the moving direction of the failure site. The size of GGFF and *h*-BN/GGFF is 5 × 3 cm^2. GGFF has graphene thickness of ~1.0 nm, and *h*-BN/GGFF has graphene and *h*-BN thickness of ~1.0 nm and ~29.5 nm, respectively. Position evolution (**f**) and moving velocity (**g**) of the failure site through the entire failure progress for the samples in **d**, **e**. The position of failure site is defined as the distance between the failure site to the "0" mark labeled in **d**, **e**, and the moving velocity is calculated as the ratio of the position change of the failure site to the duration of the failure process. **h** Stable heating durations (at ~500 °C) of *h*-BN/GGFF electrothermal devices with different *h*-BN thicknesses. The stable heating duration is defined from the point when the device reaching the saturated heating temperature (T_s), producing the maximum electric heating energy (P_0), to the point when the produced heating energy (P) decreases to 90 %*P_0. *h*-BN/GGFFs have graphene thickness of ~1.0 nm and *h*-BN thickness of 0, ~5.4, ~9.6, ~15.3, ~29.5, ~50.4 nm. **i** Stable heating durations of GGFF and *h*-BN/GGFF electrothermal devices at different heating temperatures. GGFF has a graphene thickness of ~1.0 nm, and *h*-BN/GGFF has a graphene and *h*-BN thickness of ~1.0 nm and ~29.5 nm, respectively. **j** Infrared image of *h*-BN/GGFF electrothermal device (with size of 5 × 3 cm^2) after bending ~120° at heating temperature of ~500 °C. *h*-BN/GGFF has graphene and *h*-BN thickness of ~1.0 nm and ~29.5 nm, respectively. Temperature profiles (**k**) and magnified view of heating and cooling processes (**l**) of *h*-BN/GGFF electrothermal device at different power densities, where T_s is the saturated heating temperature. **m** Temperature profile of *h*-BN/GGFF electrothermal device while applying a square wave from 0 to 120 V with period of 1 min for 1000 cycles. The error bars in **h**, **i** represent the standard deviations ($n = 5$).

indicating the doping of graphene by water. In contrast, these peaks are absent for *h*-BN/GGFF-15 (Fig. 4i), further demonstrating the role of *h*-BN layers in protecting graphene from water doping in an atmospheric environment.

To further demonstrate the effects of water on the electrical performances of GGFF and *h*-BN/GGFF in practical applications, a resistance testing device for GGFF or *h*-BN/GGFF is constructed, as shown in Fig. 4j, where the sample is conformally covered on a curved structure model, and water droplets are sprayed on it. For GGFF (Fig. 4k), the resistance significantly decreases (from ~1160 Ω to ~1037 Ω) after water spraying, suggesting that water adsorption has a noticeable impact on the electrical conduction of GGFF. This demonstrates that, like other graphene materials, GGFF is substantially influenced by the moisture during practical applications, underscoring the necessity for effective encapsulation. In contrast, for *h*-BN/GGFF (Fig. 4l), a negligible change in resistance is observed after water spraying, indicating the largely improved electrical stability of GGFF after *h*-BN encapsulation, which enhances the robustness of graphene materials during practical applications.

h-BN encapsulation enhancing high-temperature antioxidation

Graphene imparts electrical conduction to GGFF, leading to the electrothermal performance and making it highly promising for various heating applications[10,20,40,41]. However, when GGFF electrothermal device operates at a high working temperature, graphene is easily oxidized in the atmosphere[10,20,40–42], as schematically shown in Fig. 5a,

leading to the failure of the device. GGFF electrothermal device can be modeled as a resistance network comprising a series of resistance modules, and the corresponding electric power distribution of the network can be obtained by circuit simulations (Supplementary Fig. 26a). The simulation results show that a uniform resistance distribution within GGFF leads to a uniform Joule heat distribution. To demonstrate the failure progress of GGFF electrothermal device, one of the resistance modules in the resistance network is set to a higher value than the surrounding modules to simulate the defective location in GGFF, as shown in Fig. 5b. The current flowing is assumed along the warp direction of the fabric. The corresponding simulation for the electric power distribution of the network shows that the regions immediately above and below the high-resistance module produce more Joule heat (Fig. 5c), causing a localized temperature increase. This temperature rise will induce the localized oxidation of graphene, causing an increase of the local resistance. Consequently, more Joule heat is generated above and below these new-formed high-resistance regions (Supplementary Fig. 26b), elevating the local temperature and causing graphene further oxidation. This process continuously propagates, expanding perpendicularly to the current flowing direction (as labeled in Fig. 5c) and exacerbating the uneven power distribution widespread the fabric, and ultimately leads to the failure of the entire conductive network.

This failure progress of the GGFF electrothermal device is experimentally confirmed in Fig. 5d. When the device is heated to ~500 °C in atmospheric environment, localized oxidation of graphene occurs within a heating time of less than 1 s, which preferentially happens at defective areas. This graphene oxidation leads to a local temperature rise up to >800 °C, as shown in the infrared image in Fig. 5d. Then this high-temperature zone rapidly propagates perpendicular to the current direction, further exacerbating the nonuniform temperature distribution widespread the fabric. Within 3 s, the failure site propagates the entire distance of GGFF in the direction perpendicular to the current flowing, ultimately leading to the failure of the entire fabric device. Notably, *h*-BN encapsulation can effectively enhance the antioxidation of GGFF due to its higher chemical stability than graphene[36]. Figure 5e shows the failure progress of *h*-BN/GGFF electrothermal device. It can be seen that the time point when *h*-BN/GGFF begins to be oxidized comes much later than GGFF (~2000 s for *h*-BN/GGFF vs. <1 s for GGFF), and the propagating rate of the failure site on *h*-BN/GGFF is also much slower than that on GGFF.

Figure 5f quantitatively describes the position movement of the failure site over time on GGFF and *h*-BN/GGFF in Fig. 5d and e, respectively. It can be noticed that the failure site on GGFF propagates the entire fabric only in several seconds, in contrast, it requires > 3.3 hours for *h*-BN/GGFF going through this progress. The slopes for the curves in Fig. 5f reflect the propagating velocity of the failure site during the failure progress. As shown in Fig. 5g, for GGFF, the propagating velocity increases rapidly as the failure site moves forward, reaching a maximum of ~1.4 cm/s, about four orders of magnitude higher than that of *h*-BN/GGFF, which increases much more slowly, reaching a maximum of ~3.5×10^{-4} cm/s. This indicates that the failure progress of GGFF happens quite rapidly, and once local failure begins, it tends to expand swiftly, leading to widespread device failure within a short period. *h*-BN encapsulation significantly slows down the failure progress, highlighting its significant protective role in delaying the oxidation-induced failure process of graphene devices.

The stable heating duration is an important parameter to evaluate the performance of an electrothermal device. For GGFF and *h*-BN/GGFF electrothermal devices, the stable heating duration is defined from the point when the device reaching the saturated heating temperature (T_s), producing the maximum electric heating energy (P_0), to the point when the produced heating energy (P) decreases to 90 %*P_0. As shown in Fig. 5h, at ~500 °C, the stable heating duration of GGFF is typically limited to a few seconds. After *h*-BN encapsulation, this duration is significantly extended, which is highly dependent on the thickness of *h*-BN layers. With a *h*-BN thickness of ~50.4 nm, the stable heating duration of *h*-BN/GGFF can reach up to ~5 hours, which is 4 orders of magnitude higher than that of GGFF. In addition, the stable heating time of GGFF and *h*-BN/GGFF at different working temperatures are systematically compared (Fig. 5i). In the temperature range investigated (320–500 °C), the stable heating time of GGFF is very short. It can only withstand ~63 min at ~200 °C and ~10 min at ~400 °C. In contrast, for *h*-BN/GGFF with ~29.5 nm *h*-BN, the heating time is extended to ~8160 min at ~200 °C and ~1500 min at ~400 °C. However, it is worth noting that when the temperature exceeds ~400 °C, the protective effect of *h*-BN layers will be largely weakened, as *h*-BN also begins to be oxidized. Through the above analyses, *h*-BN encapsulation, especially the thick *h*-BN layers, can effectively improve the high-temperature oxidation resistance of graphene devices in the atmospheric environment.

Figure 5j shows the infrared image of *h*-BN/GGFF electrothermal device (with ~29.5 nm *h*-BN) with ~120° bending, presenting the high flexibility maintained after *h*-BN encapsulation and the uniform temperature distribution under mechanical deformation. Figure 5k and l depict the temperature profiles of *h*-BN/GGFF electrothermal device under varying power densities. During the heating stage (starting from ~10 s), the device temperature increases rapidly over time. Once the temperature stabilizes, it reaches the saturation temperature (T_s) and remains constant. In the cooling phase (starting from ~70 s), the device temperature decreases from its maximum value and eventually returns to ambient temperature. From Fig. 5l, it can be observed that the temperature rising and falling processes of the electrothermal device can be completed within ~7 s even though under relatively low input power density. For example, at a power density of ~6.18 W cm^{-2}, the temperature rising rate can reach ~174.6 °C s^{-1}. The rapid response of *h*-BN/GGFF electrothermal device is attributed to the lightweight nature and low heat capacity of the component materials. This demonstrates a significant advantage of atomic *h*-BN conformal encapsulation over traditional encapsulation methods, where the heating speed and efficiency of the device were usually largely compromised due to the thick encapsulation layers and their high heat capacity[43–45]. *h*-BN/GGFF electrothermal device exhibits electrothermal cycle stability. As shown in Fig. 5m, after applying a square wave from 0 to 120 V with a period of 1 min for 1000 cycles, the attenuation of the temperature profile is negligible.

Discussion

The encapsulation challenges posed by intricately structured graphene materials/devices are difficult to resolve with conventional whole-package encapsulation strategies, where the entire graphene layers or devices were covered as a whole, usually leading to the loss of characteristic structural features and compromising the intrinsic flexibility and portability. GGFF, characterized by a hierarchical and intricate structure, is selected as a representative platform to develop the conformal encapsulation strategy for intricately structured graphene materials/devices. In this study, high-quality, thick *h*-BN layers are in-situ grown via CVD on each graphene-covered glass fiber within GGFF. This process is particularly challenging due to the noncatalytic, nonmetallic nature of the substrate. This in-situ conformal *h*-BN encapsulation successfully unlocks the conductive network within GGFF, significantly improving its electrical stability under pressure/deformation, without sacrificing the fabric's inherent flexibility and structure. In addition, *h*-BN layers enhance the resistance of GGFF against doping and oxidation in the atmospheric environment, further improving its stability and service life. We highlight the necessity of conformal encapsulation for intricately shaped two-dimensional materials and devices, and propose a viable solution to this challenge. The proposed conformal encapsulation technology is highly universal, which can be extended to diverse two-dimensional materials

and complex device architectures. By providing a protective layer that conforms seamlessly to irregular shapes and surfaces, this technology enhances the robustness of the devices, even in challenging operational environments. This encapsulation strategy could expand the frontiers of nanoelectronics into more complex and demanding settings.

Methods

Preparation of GGFF and *h*-BN/GGFF

Graphene growth. Firstly, the GFF (QWB100P-21H4, thickness 0.10 mm, plain weave, 114 g m^{-2}) purchased from Tianjin Zhongtian Junda Glassfiber Products Co., LTD, was annealed at ~600 °C for ~2 hours in ambient air to remove the polymer coating. The pretreated GFF was loaded on a quartz plate, with a modulating plate (12 cm (length) × 5 cm (width) × 0.1 cm) positioned above it to realize the uniform growth across the hierarchical structure. The entire setup was then placed into a three-zone high-temperature tubular furnace (BTF-1200C-III, AnHui BEQ Equipment Technology Co., Ltd., China). Then, the CVD chamber was flushed with 100 sccm argon (Ar) under atmospheric pressure and heated to the desired graphene growth temperature. Then turned off Ar. The typical graphene growth process on GFF was performed under 10–30 sccm methane (CH_4), which was the carbon source, 100 sccm H_2, at the growth temperature of ~1100 °C for 1–10 hours. Subsequently, the heating and CH_4 gas were turned off, and 100 sccm Ar was introduced into the CVD chamber. The chamber began to cool down, during which 100 sccm Ar and 100 sccm H_2 were maintained. Once the chamber reached room temperature, the Ar and H_2 were turned off.

***h*-BN growth**. After the graphene growth progress finished, *h*-BN growth was conducted with the low-pressure CVD (LPCVD) system. First, the CVD system was evacuated to a base pressure of <1 Pa and heated to 1100 °C under 50 sccm H_2 and 100 sccm Ar. The ammonia borane (NH_3BH_3) (97 % purity, from Sigma-Aldrich) was placed in a tube connected to the front end of the CVD system, which was heated to 70–100 °C by a program-controlled heating belt. The flows of 50 sccm H_2 and 100 sccm Ar were maintained to transport volatile precursor for *h*-BN growth on GGFF. This progress usually lasts 0.5–4 hours. After *h*-BN growth, the NH_3BH_3 supply was stopped, and the furnace was cooled down to room temperature under the flow of 50 sccm Ar and 100 sccm H_2. The preparation diagram of the CVD process is shown in Supplementary Fig. 1.

Characterization

The prepared samples were characterized using SEM (Thermo Scientific Quattro S, acceleration voltage: 20 kV), Raman spectroscopy (Horiba, LabRAM HR800, 532 nm laser excitation, 50×objective lens), atomic force microscope (AFM) (Bruker Dimension Icon with ScanAsyst mode), and HR-TEM (JEM-ARM200F NEOARM, 200 kV). XPS (Kratos Analytical Axis-Ultra spectrometer with Al Kα X-ray source). The sheet resistance was measured by a four-point probe resistivity measurement system (RTS-8). The current, voltage, and resistance values of electronic devices were recorded with a Keithley 2450 digital Sourcemeter.

Transfer process of graphene layers and *h*-BN/graphene layers

GGFs or *h*-BN/GGFs were drawn from the selected position of the GGFF or *h*-BN/GGFF samples using tweezers. Cut GGFs or *h*-BN/GGFs into small pieces using scissors. Then disperse them in HF solution (50%) to remove the inner glass fibers. After a few hours, the internal glass fibers were etched away, and GGFs or *h*-BN/GGFs collapsed into graphene or *h*-BN/graphene ribbons. Then the ribbons were cleaned three times with deionized water. Finally, the graphene or *h*-BN/graphene ribbons were loaded with silicon wafers and dried with infrared light.

Fabrications of electronic test devices based on GGFF, *h*-BN/GGFF, PI/GGFF, and PI/*h*-BN/GGFF

To investigate the effects of different encapsulation strategies (*h*-BN conformal encapsulation and PI film whole-package encapsulation) on the electrical stability of GGFF, the electronic test devices based on GGFF, *h*-BN/GGFF, PI/GGFF, and PI/*h*-BN/GGFF were constructed (Supplementary Fig. 23). For GGFF electronic test device, copper double-sided tape is attached to both ends of the GGFF sample as electrodes. For *h*-BN/GGFF, during *h*-BN growth, the positions on GGFF where the electrodes would be placed were blocked to avoid *h*-BN deposition. Then the copper electrodes were affixed on both ends of *h*-BN/GGFF sample, where no *h*-BN was covered. PI/GGFF and PI/*h*-BN/GGFF samples were obtained by covering the PI film onto the above-obtained GGFF and *h*-BN/GGFF electronic test devices. The steps of PI film encapsulation are as follows: (1) The PI film was cut into a size slightly larger than that of the GGFF and *h*-BN/GGFF samples. (2) Place the PI film on the top and bottom of GGFF or *h*-BN/GGFF to form a sandwich-like structure. (3) Heat presses the above samples at ~150 °C for ~20 seconds. (4) After pressing, let the samples cool to room temperature.

Finally, connect the copper wire to the copper double-sided tape electrode, ensuring a firm contact between the copper wire and the tape to maintain a stable electrical connection. Connect the power supply, then the resistance of GGFF, *h*-BN/GGFF, PI/GGFF, and PI/*h*-BN/GGFF based electronic test devices were monitored.

Fabrication of electrothermal devices based on GGFF and *h*-BN/GGFF

To study the effect of *h*-BN encapsulation on the high-temperature antioxidant properties of GGFF in the atmospheric environment and the performance of *h*-BN/GGFF electrothermal devices, electrothermal devices based on GGFF and *h*-BN/GGFF were constructed. The fabrications of the GGFF and *h*-BN/GGFF electrothermal devices were similar to the construction of electronic test devices as illustrated above. After devices construction finished, connect the DC power supply, the infrared images of GGFF and *h*-BN/GGFF electrothermal devices were monitored by a Fluke Ti 10 infrared thermal imager.

Data availability

The Source Data underlying the figures of this study are available with the paper. All raw data generated during the current study are available from the corresponding authors upon request. Source data are provided with this paper.

References

1. Chen, D., Tang, L. & Li, J. Graphene-based materials in electrochemistry. *Chem. Soc. Rev.* **39**, 3157–3180 (2010).
2. Das, A. et al. Monitoring dopants by Raman scattering in an electrochemically top-gated graphene transistor. *Nat. Nanotechnol.* **3**, 210–215 (2008).
3. Jose, S. A. Design and fabrication of highly sensitive graphene-based sensors for environmental and health monitoring applications. Doctoral Thesis, School of Electronics, Electrical Engineering and Computer Science, Queen's University Belfast (2024).
4. Petrone, N. et al. Chemical vapor deposition-derived graphene with electrical performance of exfoliated graphene. *Nano Lett.* **12**, 2751–2756 (2012).
5. Qing, F. et al. Towards large-scale graphene transfer. *Nanoscale* **12**, 10890–10911 (2020).
6. Bounos, G. et al. Enhancing water vapor permeability in mixed matrix polypropylene membranes through carbon nanotubes dispersion. *J. Membr. Sci.* **524**, 576–584 (2017).
7. Wang, L. et al. Application challenges in fiber and textile electronics. *Adv. Mater.* **32**, 1901971 (2020).

8. Jen, S.-H., Bertrand, J. A. & George, S. M. Critical tensile and compressive strains for cracking of Al_2O_3 films grown by atomic layer deposition. *J. Appl. Phys.* **109**, 084305 (2011).
9. Yong-Qiang, Y. & Yu, D. Optimization of Al_2O_3 films deposited by ald at low temperatures for oled encapsulation. *J. Phys. Chem. C.* **118**, 18783–18787 (2014).
10. Jiang, J. et al. Flexible full-surface conformal encapsulation for each fiber in graphene glass fiber fabric against thermal oxidation. *ACS Appl. Mater. Interfaces* **14**, 19889–19896 (2022).
11. Meiyazhagan, A. et al. Gas-phase fluorination of hexagonal boron nitride. *Adv. Mater.* **33**, 2106084 (2021).
12. Yang, Y. et al. Intrinsic toughening and stable crack propagation in hexagonal boron nitride. *Nature* **594**, 57–61 (2021).
13. Mariello, M., Kim, K., Wu, K., Lacour, S. P. & Leterrier, Y. Recent advances in encapsulation of flexible bioelectronic implants: Materials, technologies, and characterization methods. *Adv. Mater.* **34**, 2201129 (2022).
14. Liu, R. et al. Controllable preparation of graphene glass fiber fabric towards mass production and its application in self-adaptive thermal management. *Sci. Bull.* **69**, 2712–2722 (2024).
15. Liu, R. et al. Complementary chemical vapor deposition fabrication for large-area uniform graphene glass fiber fabric. *Small Methods* **6**, 2200499 (2022).
16. Wang, K. et al. Multispecies-coadsorption-induced rapid preparation of graphene glass fiber fabric and applications in flexible pressure sensor. *Nat. Commun.* **15**, 5040 (2024).
17. Cheng, Y. et al. Graphene infrared radiation management targeting photothermal conversion for electric-energy-free crude oil collection. *J. Am. Chem. Soc.* **144**, 15562–15568 (2022).
18. Xie, Y. et al. Ultra-broadband strong electromagnetic interference shielding with ferromagnetic graphene quartz fabric. *Adv. Mater.* **34**, 2202982 (2022).
19. Yuan, H. et al. Scalable fabrication of dual-function fabric for zero-energy thermal environmental management through multiband, synergistic, and asymmetric optical modulations. *Adv. Mater.* **35**, 2209897 (2023).
20. Yuan, H. et al. Dual-emitter graphene glass fiber fabric for radiant heating. *ACS Nano* **16**, 2577–2584 (2022).
21. Li, L. H., Cervenka, J., Watanabe, K., Taniguchi, T. & Chen, Y. Strong oxidation resistance of atomically thin boron nitride nanosheets. *ACS Nano* **8**, 1457–1462 (2014).
22. Sun, J. et al. Recent progress in the tailored growth of two-dimensional hexagonal boron nitride via chemical vapour deposition. *Chem. Soc. Rev.* **47**, 4242–4257 (2018).
23. Liu, H. et al. Synthesis of hexagonal boron nitrides by chemical vapor deposition and their use as single photon emitters. *Nano Mater. Sci.* **3**, 291–312 (2021).
24. Ma, K. Y., Kim, M. & Shin, H. S. Large-area hexagonal boron nitride layers by chemical vapor deposition: Growth and applications for substrates, encapsulation, and membranes. *Acc. Mater. Res.* **3**, 748–760 (2022).
25. Kim, J. et al. Conformal growth of hexagonal boron nitride on high-aspect-ratio silicon-based nanotrenches. *Chem. Mater.* **35**, 2429–2438 (2023).
26. Roy, S. et al. Structure, properties and applications of two-dimensional hexagonal boron nitride. *Adv. Mater.* **33**, 2101589 (2021).
27. Jang, A.-R. et al. Wafer-scale and wrinkle-free epitaxial growth of single-orientated multilayer hexagonal boron nitride on sapphire. *Nano Lett.* **16**, 3360–3366 (2016).
28. Behura, S., Nguyen, P., Che, S., Debbarma, R. & Berry, V. Large-area, transfer-free, oxide-assisted synthesis of hexagonal boron nitride films and their heterostructures with MoS_2 and WS_2. *J. Am. Chem. Soc.* **137**, 13060–13065 (2015).
29. Decker, J. J. et al. Polyethylene-based nanocomposites containing organoclay: A new approach to enhance gas barrier via multilayer coextrusion and interdiffusion. *Polymer* **61**, 42–54 (2015).
30. Yousefi, N. et al. Highly aligned, ultralarge-size reduced graphene oxide/polyurethane nanocomposites: Mechanical properties and moisture permeability. *Compos. - A: Appl. Sci. Manuf.* **49**, 42–50 (2013).
31. Takei, K. et al. Nanowire active-matrix circuitry for low-voltage macroscale artificial skin. *Nat. Mater.* **9**, 821–826 (2010).
32. Atalay, O. & Kennon, W. R. Knitted strain sensors: Impact of design parameters on sensing properties. *Sensors* **14**, 4712–4730 (2014).
33. Melios, C., Giusca, C. E., Panchal, V. & Kazakova, O. Water on graphene: Review of recent progress. *2D Mater.* **5**, 022001 (2018).
34. Melios, C. et al. Effects of humidity on the electronic properties of graphene prepared by chemical vapour deposition. *Carbon* **103**, 273–280 (2016).
35. Melios, C. et al. Tuning epitaxial graphene sensitivity to water by hydrogen intercalation. *Nanoscale* **9**, 3440–3448 (2017).
36. Yang, X., Zhang, R., Pu, J., He, Z. & Xiong, L. 2D graphene and *h*-BN layers application in protective coatings. *Corros. Rev.* **39**, 93–107 (2021).
37. Panchal, V. et al. Atmospheric doping effects in epitaxial graphene: Correlation of local and global electrical studies. *2D Mater.* **3**, 015006 (2016).
38. Kwon, K. C., Choi, K. S., Kim, C. & Kim, S. Y. Effect of transition-metal chlorides on graphene properties. *Phys. Status Solidi A* **211**, 1794–1800 (2014).
39. Lin, L. et al. Towards super-clean graphene. *Nat. Commun.* **10**, 1912 (2019).
40. Huang, K. et al. Overcoming the incompatibility between electrical conductivity and electromagnetic transmissivity: A graphene glass fiber fabric design strategy. *Adv. Mater.* **36**, 2313752 (2024).
41. Qi, Y., Sun, L. & Liu, Z. Super graphene-skinned materials: An innovative strategy toward graphene applications. *ACS Nano* **18**, 4617–4623 (2024).
42. Fang, B., Chang, D., Xu, Z. & Gao, C. A review on graphene fibers: Expectations, advances, and prospects. *Adv. Mater.* **32**, 1902664 (2020).
43. Kang, J. et al. High-performance graphene-based transparent flexible heaters. *Nano Lett.* **11**, 5154–5158 (2011).
44. Liu, P., Liu, L., Jiang, K. & Fan, S. Carbon-nanotube-film microheater on a polyethylene terephthalate substrate and its application in thermochromic displays. *Small* **7**, 732–736 (2011).
45. Sui, D. et al. Flexible and transparent electrothermal film heaters based on graphene materials. *Small* **7**, 3186–3192 (2011).

Acknowledgements

This work was financially supported by the National Natural Science Foundation of China (NSFC, Nos. 52272032, T2188101, 52021006 to Y.Q. and Z.F.L.).

Author contributions

X.M.Y., Y.Y.Y., and S.T.C. conceived the project and designed the experiment. Y.Y.Y. and X.M.Y. performed the CVD growth of materials. X.M.Y., Y.Y.Y., S.T.C. fabricated the devices with assistance from H.Y., X.Z.G., W.J.L., F.S.L., F.Y. All measurements were made by X.M.Y., S.T.C., with the assistance of K.Y.Z., L.F.L., W.J.J., Q.X.S., X.Y.M., J.N.W., Y.J.Z., E.S.L.; X.M.Y., Y.Y.Y., S.T.C. co-wrote the paper under the guidance of Y.Q. and Z.F.L. All authors contributed to the discussion and analysis of the results.

Competing interests

The authors declare no competing interests.

Additional information

Supplementary information The online version contains supplementary material available at https://doi.org/10.1038/s41467-025-60324-0.

Correspondence and requests for materials should be addressed to Zhongfan Liu or Yue Qi.

Peer review information *Nature Communications* thanks Dmitry (S) Muratov and the other anonymous reviewers for their contribution to the peer review of this work. A peer review file is available.